AIAA AVIATION Forum
June 15-19, 2020, VIRTUAL EVENT
AIAA AVIATION 2020 FORUM

10.2514/6.2020-2954

Mitigation of Serpentine Duct Flow Distortion Using Co-Flow Jet Active Flow Control

Kewei Xu *, Gecheng Zha †
Dept. of Mechanical and Aerospace Engineering
University of Miami, Coral Gables, Florida 33124
E-mail: gzha@miami.edu

Abstract

This paper implements Co-flow Jet (CFJ) active flow control (AFC) on the M2129 serpentine duct for mitigating flow separation with low energy consumption. Various locations and slot widths of CFJ suction duct are studied and the energy expenditure of each case is analyzed. The 3D Reynolds Averaged Navier-Stokes (RANS) equations with one-equation Spalart-Allmaras turbulence model is used. The experimental data of AGARD test case 3.1, which has throat Mach number of 0.79, is used for validation. The predicted total pressure recovery agrees very well with the experiment with the discrepancy of less than 1%. The distortion coefficient (DC_{60}) is also in an acceptable agreement with the experiment. The simulation result is further validated using the wall static pressure distribution, which also achieves a good agreement with the experiment. For the CFJ S-duct, a horn shaped slot geometry is adopted for the CFJ injection and suction slots to minimize the separation caused by CFJ sides wall. For the optimum configuration of the CFJ S-duct, a small distortion coefficient of 1.7% is achieved with the averaged total pressure recovery increased by 1.9%. The optimum CFJ configuration is able to substantially reduce the required CFJ power consumption due to placing the suction at the geometric inflection point. Overall, the CFJ active flow control is demonstrated numerically to be very effective to mitigate the S-duct flow distortion and improve total pressure recovery.

Nomenclature

AFC	Active flow control
AIP	Aerodynamic Interface Plane
CFJ	Co-flow jet
DC_{60}	Distortion coefficient of 60 degree, $DC_{60} = \frac{Pt_{AIP} - Pt_d}{q_d}$
Ma	Mach number
P	Power consumption of CFJ actuator
Pt_{AIP}	Averaged total pressure at AIP
Pt_d	Averaged total pressure at distortion section
q_d	Averaged dynamic pressure at AIP
R_i	Radius of the S-duct inlet
Re	Reynolds number
X	Axial location
$ZNMF$	Zero-net mass flux

* Ph.D. candidate
† Professor, ASME Fellow, AIAA associate Fellow

c	Subscript, stands for corrected
j	Subscript, stands for jet
β	Circumferential angle of CFJ duct
γ	Air specific heats ratio
δ	Total pressure recovery ratio
Γ	Pressure ratio
η	Micro-comprssor efficiency
θ	Circumferential angle of S-duct

1 Introduction

Serpentine ducts (S-ducts) are widely studied for modern aircraft. Combined with boundary layer ingestion, a short S-duct is able to significantly reduce the fuel consumption and ram drag [1, 2]. For the military aircraft, S-ducts also reduce radar cross-sectional visibility due to the buried engines [3, 4]. However, a major challenge of S-ducts is the flow distortion caused by flow separation, which is often induced by the high curvature wall at duct bend. The consequences can be severe, such as reducing compressor stall margin and efficiency, exciting fan blade high cycle fatigue vibration, decreasing aircraft maneuverability and engine life span, etc.

To mitigate the flow separation inside S-ducts, passive flow control using vortex generators (VG) is studied numerically and experimentally by other researchers [5, 6, 7, 8]. For the CFD simulated vortex generators, the engine face distortion and flow unsteadiness of M2129 S-duct is reduced up to 80% [9]. Jirasek et al [10] conduct an optimization study of vortex generator and find the effectiveness mainly depends on height and its location in the flow separation zone. Yi et al [11] independently optimize the vortex generators based on the discrete adjoint approach, and is able to reduce the DC_{60} to 0.9%.

For active flow control, fluidic-oscillating jets [12, 13] are used on a serpentine offset diffuser to generate streamwise vorticity and reduce total pressure distortion. It is able to reduce the Aerodynamic Interface Plane (AIP) distortion by more than 60%. Harrison et al [14, 15] propose an ejector-pump concept to employ injection and suction simultaneously. It reduces the demand for bleed air from the compressor. With the ejector-pump model, the maximum reduction of engine-face distortion of 75% is achieved. Rudin et al [16] also apply steady suction and blowing on the S-duct of a Blended Wing-Body (BWB) and achieve an improvement of 4.3% in total pressure recovery and 70% in DC_{60} reduction. Even though passive flow controls such as VG appear to be very effective to reduce the S-Duct distortion [11], active flow controls that transfer energy to the main flow in general will have more control effectiveness for broader flow conditions and applications.

The Co-flow Jet (CFJ) active flow control [17, 18, 19, 20, 21, 22, 23, 24, 25, 26, 27] is demonstrated to be very effective and efficient for airfoil flow control to achieve ultra-high lift coefficient, stall angle of attack, and drag reduction. The CFJ is a zero-net-mass-flux flow control with a very low energy expenditure. Recently, Xu et al [28, 29, 30, 31] apply the CFJ to the NASA hump and flight control surfaces with very high effectiveness and energy efficiency for removing separation. The purpose of this paper is to make the first attempt to apply the Co-flow Jet (CFJ) active flow control (AFC) to a serpentine duct to largely remove flow distortion with low energy expenditure.

2 The Co-flow Jet Parameters

To facilitate the description of CFJ control surface performance, a few important parameters are given below.

2.1 Jet Momentum Coefficient

The injection jet momentum coefficient C_μ is used to describe the CFJ strength as:

$$C_\mu = \frac{\dot{m} V_j}{\frac{1}{2}\rho_\infty {V_\infty}^2 A_{ref}} \tag{1}$$

where $\dot{m}$ is the injection mass flow, V_j is the mass-averaged injection velocity, ρ_∞ and V_∞ denote the free stream density and velocity, and A_{ref} is the reference area defined as inlet area of the S-duct.

2.2 Power Coefficient

The CFJ power required is determined by the total enthalpy rise from the suction duct outlet to the injection duct inlet [32]. The total enthalpy rise can be achieved by the embedded micro-compressors. The power required by the CFJ can be expressed as:

$$P = \frac{\dot{m} H_{t2}}{\eta}(\Gamma^{\frac{\gamma-1}{\gamma}} - 1) \tag{2}$$

where, $\dot{m}$ is the CFJ mass flow rate, H_{t2} is the total enthalpy at the suction slot, Γ is the total pressure ratio between the injection and suction, and η is the pumping system efficiency.

Eq. (2) indicates that the power required by the CFJ is linearly determined by the mass flow rate and exponentially by the total pressure ratio. This relationship in fact applies to all the active flow controls based on fluidic actuators. Thus, C_μ can not be used to represent the power consumption of active flow control [32, 33]. For example, a high C_μ could have a substantially lower power consumption than a smaller C_μ if the large C_μ is created by a high mass flow rate and low jet velocity, which only requires a significantly lower total pressure ratio [33, 34]. The power coefficient is defined as:

$$P_c = \frac{P}{\frac{1}{2}\rho_\infty V_\infty^3 A_{ref}} \tag{3}$$

where P is the CFJ required power defined in Eq. (2).

3 The Numerical Algorithm

The in-house high order accuracy CFD code Flow-Acoustics-Structure Interaction Package (FASIP) is used to conduct the numerical simulation. The 3D Reynolds Averaged Navier-Stokes (RANS) equations with one-equation Spalart-Allmaras [35] turbulence model is used. A 3rd order WENO scheme for the inviscid flux [36, 37, 38] and a 2nd order central differencing for the viscous terms are employed to discretize the Navier-Stokes equations. The low diffusion E-CUSP scheme used as the approximate Riemann solver suggested by Zha et al [39] is utilized with the WENO scheme to evaluate the inviscid fluxes. Implicit time marching method using Gauss-Seidel line relaxation is

used to achieve a fast convergence rate [40]. Parallel computing is implemented to save wall clock simulation time [41]. The FASIP code is intensively validated for CFJ flow control simulations [18, 19, 20, 21, 24, 25, 26, 42, 43, 44].

4 Baseline Serpentine Duct Validation

The baseline serpentine duct (S-duct) studied in the present research with the side-view shown in Fig. 1 is adopted from [45]. The throat is located at the origin point of the axial axis. The duct is tested experimentally in the AGARD study [46]. The S-duct is approximately 2 ft in length and the throat is 0.4225 ft in diameter, which is located at the end of the upstream constant-area section. The outlet diameter is 0.5 ft with a diverging area ratio of outlet to inlet of 1.4. The engine face, or the aerodynamic interface plane (AIP), is located at 1.6 ft downstream of the duct throat. The duct inlet conditions for the simulation are adopted from the AGARD test cases, which have total pressure of 101,216 Pa, total temperature of 293 K and Re of 2.36 million. The inlet velocity is imposed to be normal to the inlet surface.

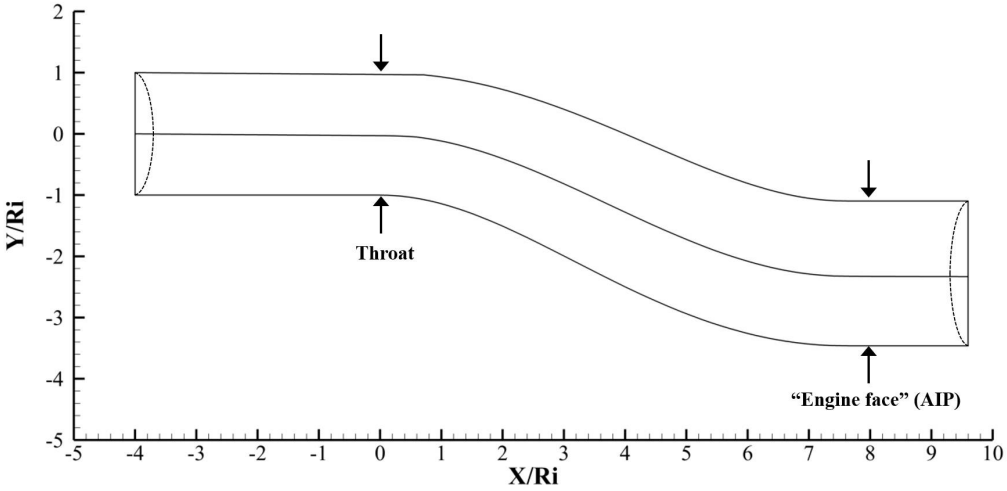

Figure 1: Side-view of the baseline S-duct

The mesh topology is shown in Fig. 2. Only half of the S-duct is simulated due to the symmetric geometry. The S-duct bend section is refined and a butterfly grid treatment is used for the duct cross-section meshing as shown in Fig. 2 (left). The overall mesh size is 2.0 million points. The boundary condition at the S-duct inlet has the specified total pressure, total temperature and flow angle. The outlet boundary condition uses a specified static pressure. Non-slip wall boundary condition is enforced on the duct wall and symmetry boundary condition is applied on the S-duct symmetric plane. The center-body of the S-duct at the downstream of the AIP is not simulated.

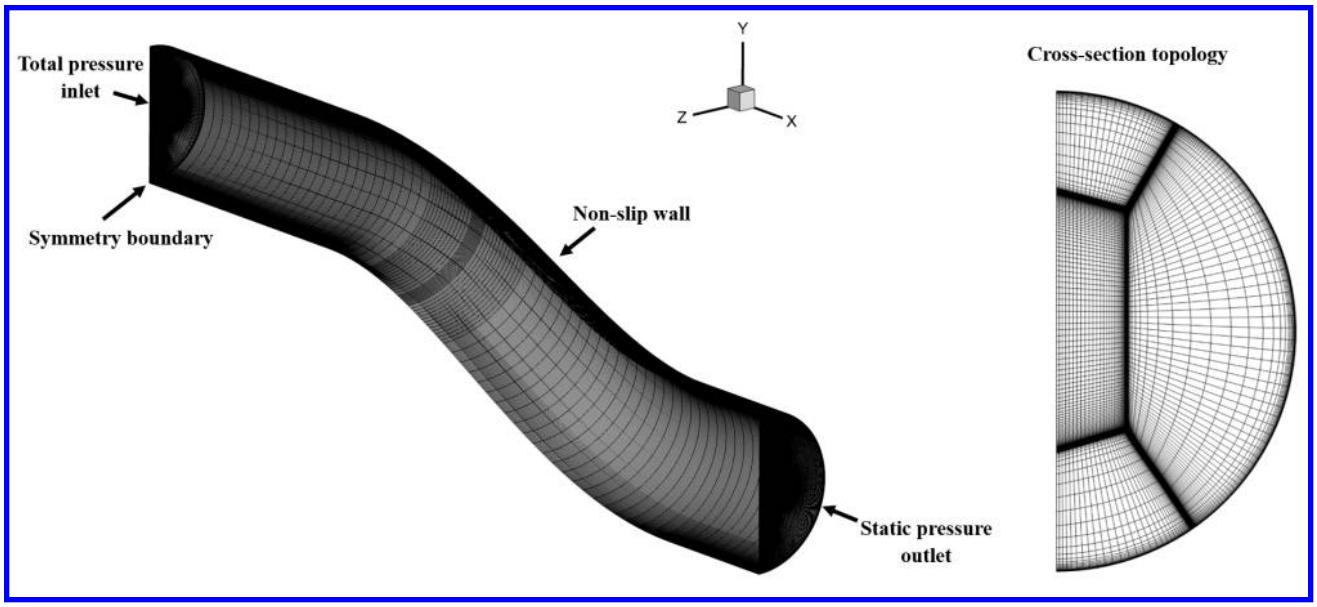

Figure 2: Mesh topology of the baseline S-duct

The plot on the left of Fig. 3 shows the Mach contours of the baseline S-duct at the symmetric plane with the throat Mach number (Ma_{th}) of 0.79. The plot on the right of Fig. 3 shows the distribution of total pressure recovery at AIP. Massive flow separation occurs at the duct bend section, which causes significant total pressure loss and distortion at the bottom of AIP. With the throat Mach number of 0.79, the predicted total pressure recovery is 95.3%, which has a less than 1% discrepancy from the experimental value of 95.7%. The predicted distortion coefficient DC_{60} at AIP is 43.2% and has a deviation from the measured value of 40.4% by about 6.9%, which is considered due to missing the center-body in the simulation as reported by other researchers [47, 48]. The DC_{60} [49] is the distortion coefficient computed based on a sector of 60° as shown in Fig. 3. The distortion sector with a 60° is usually considered as an required range [49]. The formulation of DC_{60} is the following,

$$DC_{60} = \frac{Pt_{AIP} - Pt_d}{q_d} \tag{4}$$

Where the Pt_{AIP} is area-averaged total pressure at AIP, Pt_d is area-averaged toal pressure in the worst 60 degree sector of the engine face, and q_d is averaged dynamic pressure at AIP. Since the Pt_d is in the distortion area suffering more loss, the value should be lower the Pt_{AIP}.

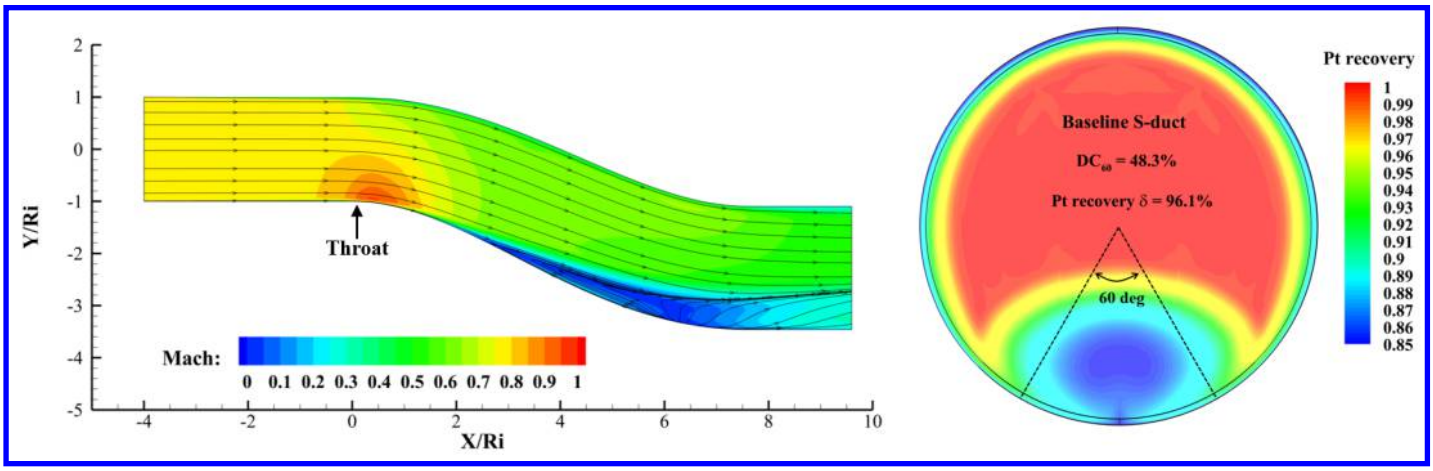

Figure 3: Mach contour of the baseline S-duct and total pressure recovery at AIP

Fig.4 shows the top (θ=0°) and bottom (θ=180°) wall surface static pressure distribution in the axial direction. A very good overall agreement is achieved between the predicted results and experiment with the maximum discrepancy of 4.8%. The deviation is mostly at the bottom surface, which has the flow separation due to S-duct bend.

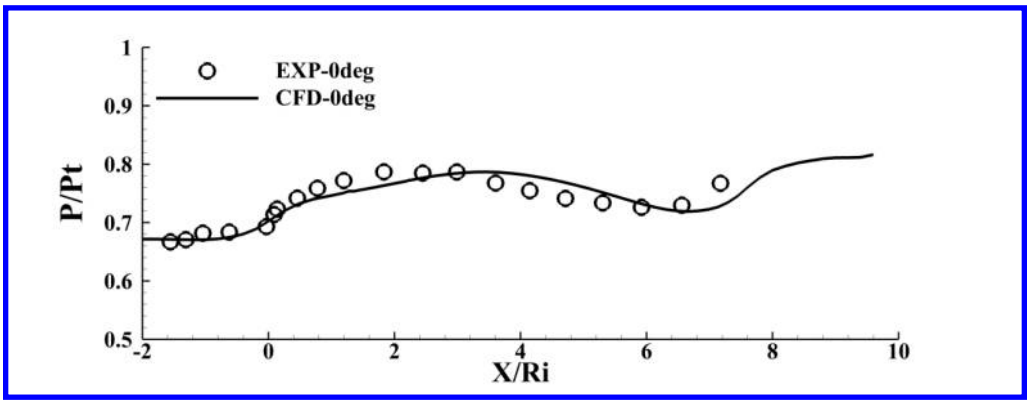

(a) 0°, top surface

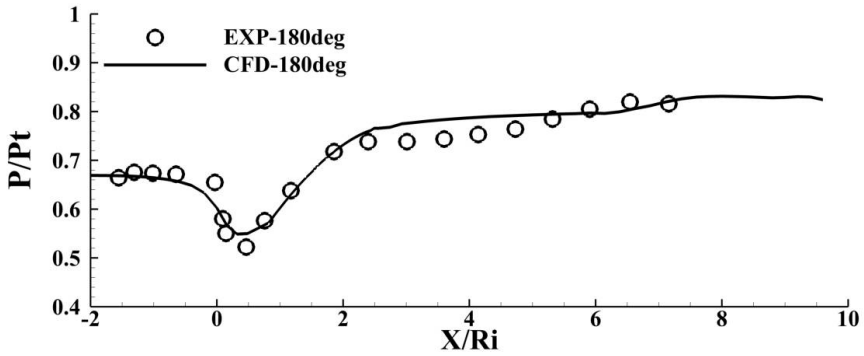

(b) 180°, bottom surface

Figure 4: Wall static pressure distributions

5 CFJ Serpentine Duct Geometry

One of the CFJ S-duct configurations is shown in Fig. 5 to illustrate how the CFJ is incorporated with the S-duct. The CFJ S-duct is created by placing an injection slot (in blue) at the start of the duct turning immediately downstream of the throat and placing a suction slot (in orange) in the downstream of duct bend. The injection jet enters the duct tangentially to the local wall surface. The same amount of mass flow is withdrawn smoothly into the suction duct. To make the injection and suction smooth, the bottom wall surface is translated radially outward by a concentric circle with the radius increased by 0.5% of the inlet radius. The CFJ will energize the boundary layer to sustain the adverse pressure gradient of the duct diffusion and make the flow attached. The circumferential horn shaped slot geometry (shown in gray) is adopted for the CFJ injection and suction slots to minimize the separation caused by the CFJ duct wall on the both sides. A circumferential width of the slot of CFJ ducts is expressed by its circumferential angle (β) in Fig. 5.

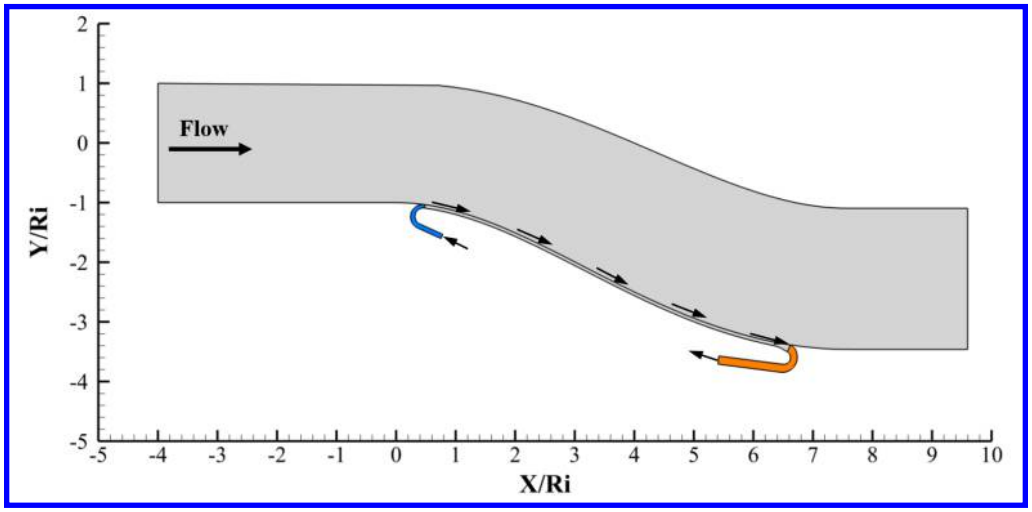

(a) CFJ S-duct at symmetric plane view

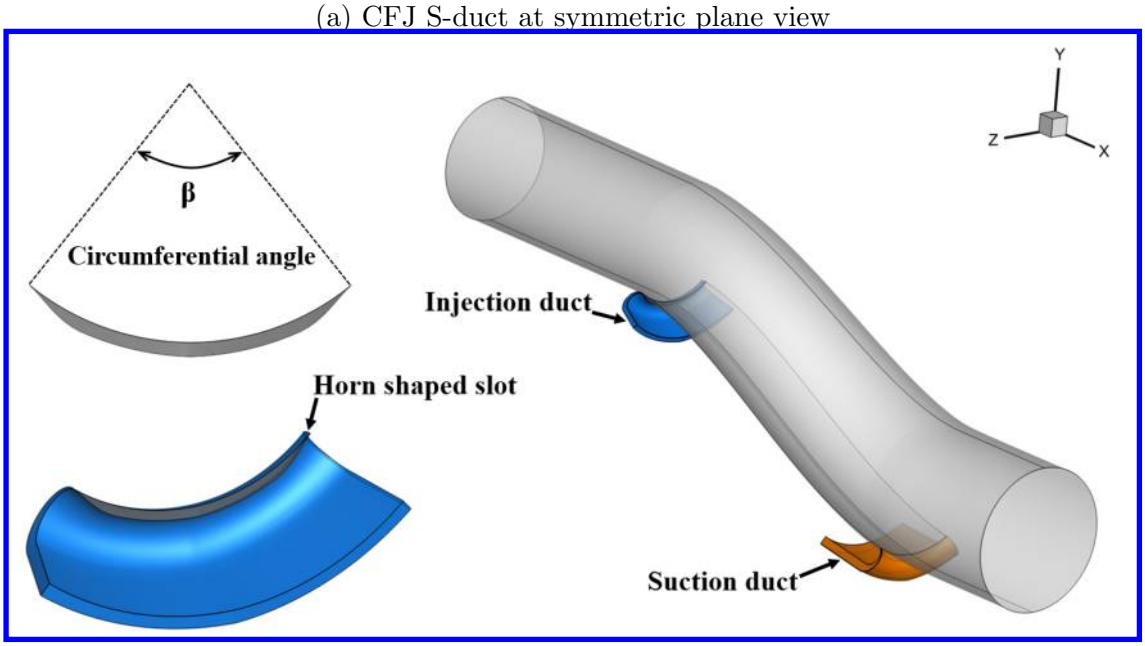

(b) 3D geometry of CFJ S-duct

Figure 5: Illustration of CFJ S-duct

6 Results

Four configurations of the CFJ S-ducts with two circumferential angles (β) of injection and suction slots, and two suction locations are simulated for the trade study. The injection location is fixed at 0.47 X/R_i (axial coordinate normalized by the inlet radius). More details of the geometrical parameters are presented in Table 1. Case 1 and 2 have the same circumferential width β angle for the injection and suction slot, but the suction slot axial location is different. Case 1 has the suction located at more downstream at X/R_i=6.63. Case 2 has the suction located more upstream at X/R_i=3.29. The comparison of Case 1 and 2 can show the effect of the suction slot. Case 3 has the same suction location as Case 1 and Case 4 has the same suction location as Case 2. Compared with Case 1 and 2, Case 3 and 4 increase the circumferential width angle by 20° for both the injection and suction slot to cover more CFJ influence area. This comparison is to show the effect of the CFJ slot width. For all the cases, the injection width angle is 10° more than that of the suction slot to make the two slots aligned at the same span position from the top projection view. This is because the radius at the AIP is greater than that immediate downstream of the throat. Making the slot corner aligned is intended to facilitate the suction slot to absorb all the injection flow. This choice is based on some preliminary trails and is not necessarily the optimum configuration.

Table 1: Geometrical parameters of CFJ S-ducts

Cases	Inj Location (X/R_i)	Suc Location (X/R_i)	Inj β (°)	Suc β (°)
1	0.47	6.63	80	70
2	0.47	3.29	80	70
3	0.47	6.63	100	90
4	0.47	3.29	100	90

Fig. 6 shows the Mach number contours and streamlines at the symmetric plane for the CFJ S-ducts with suction β of 70°. The separation in CFJ S-duct is removed. It is observed that a high speed jet is injected through the injection duct and energizes the main flow to overcome the adverse pressure gradient at S-duct bend. For the distortion coefficient, Case 2 is 35% lower than Case 1 because of the suction location difference. Detailed reasons will be discussed later with Case 3 and Case 4.

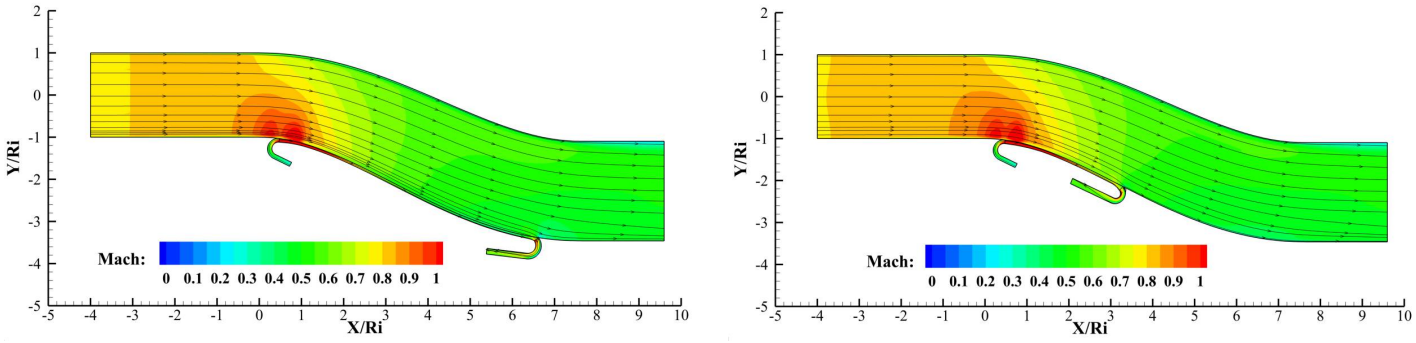

(a) Case 1, suction at 6.63 X/R_i

(b) Case 2, suction at 3.29 X/R_i

Figure 6: Mach contours of the CFJ S-ducts at symmetry view, suction β=70°

Fig. 7 shows the cross sectional total pressure contours in the stream-wise of CFJ S-ducts with the suction β of 70°. The total pressure is normalized by the inlet density and velocity. A high energy flow with high total

pressure is injected through the injection duct. As flow approaches downstream, the high energy jet mixes with the retarded main flow at the duct bend and energizes the boundary layer. Since the flow separation is removed as shown in Fig. 6 and Fig. 7, the DC_{60} is significantly reduced as shown in Fig. 8. However, there is a low total pressure region at the 5 o'clock position at the AIP as shown in Fig. 8. As observed by Yi et al [11], this part of the low energy flow (marked as Flow 1) migrates from the inlet on the duct-side as shown in Fig. 9, which is driven by the static pressure difference between the top wall and the bottom wall of S-duct. At the same time, the non-uniform injection through the CFJ injection slot horn appears to be too weak to energize this part of the flow. More study will be done to investigate how to essentially eliminate this low energy flow area by changing the CFJ slot such as the width, corner shape, injection strength, etc.

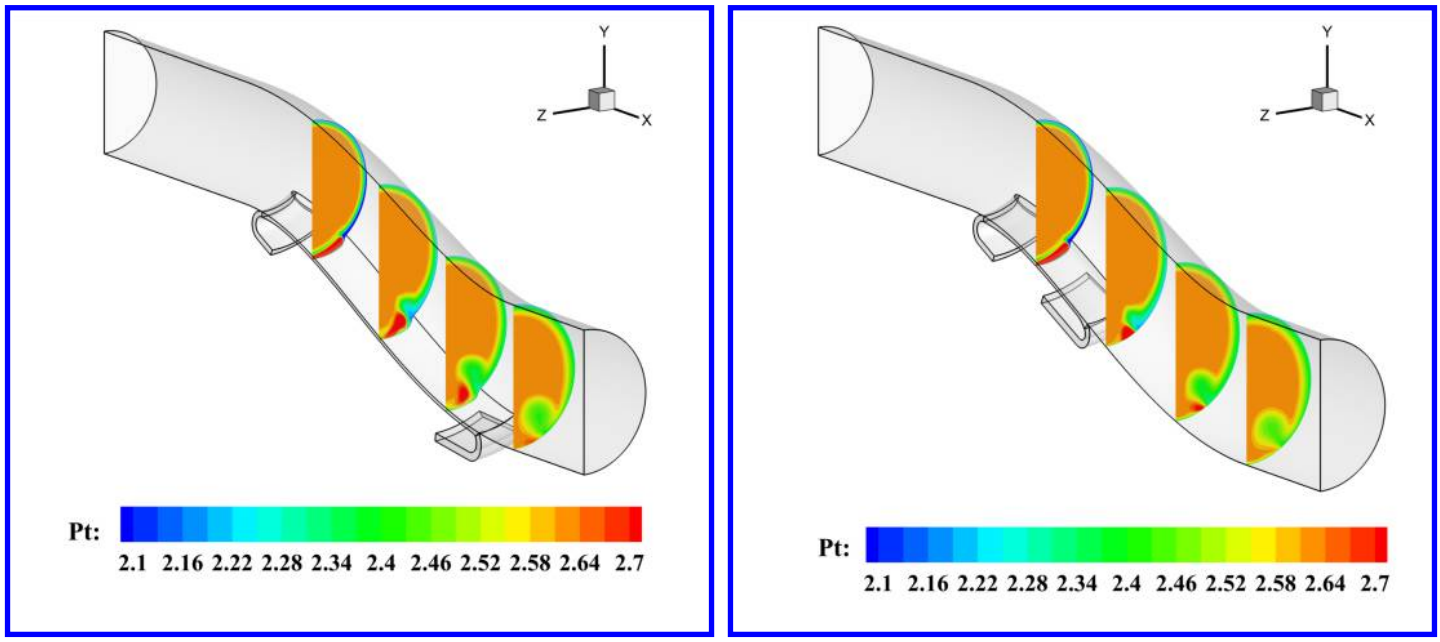

(a) Case 1, suction at 6.63 X/R_i (b) Case 2, suction at 3.29 X/R_i

Figure 7: Total pressure contours along stream-wise of CFJ S-ducts, suction β=70 °

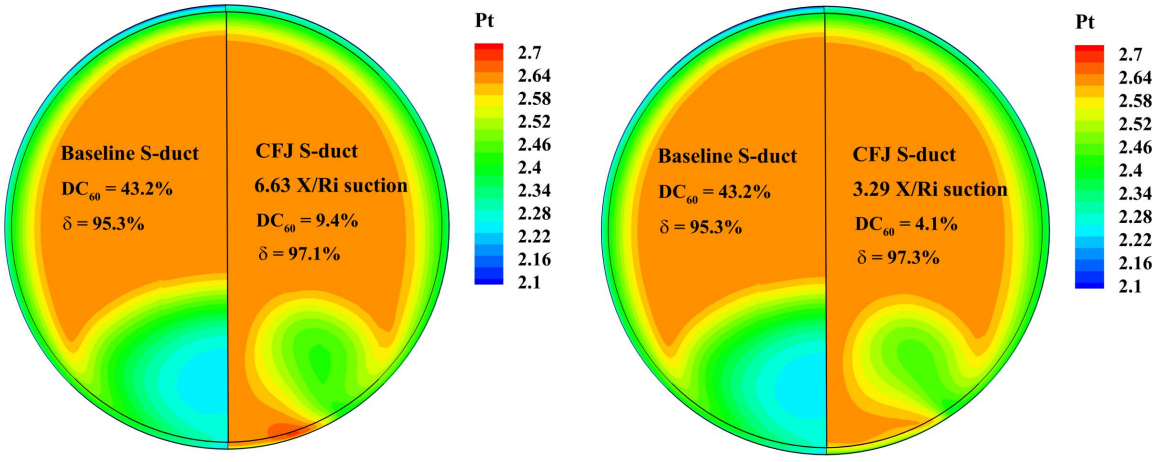

(a) Case 1, suction at 6.63 X/R_i (b) Case 2, suction at 3.29 X/R_i

Figure 8: Total pressure contours at AIP of CFJ S-ducts, suction β=70°

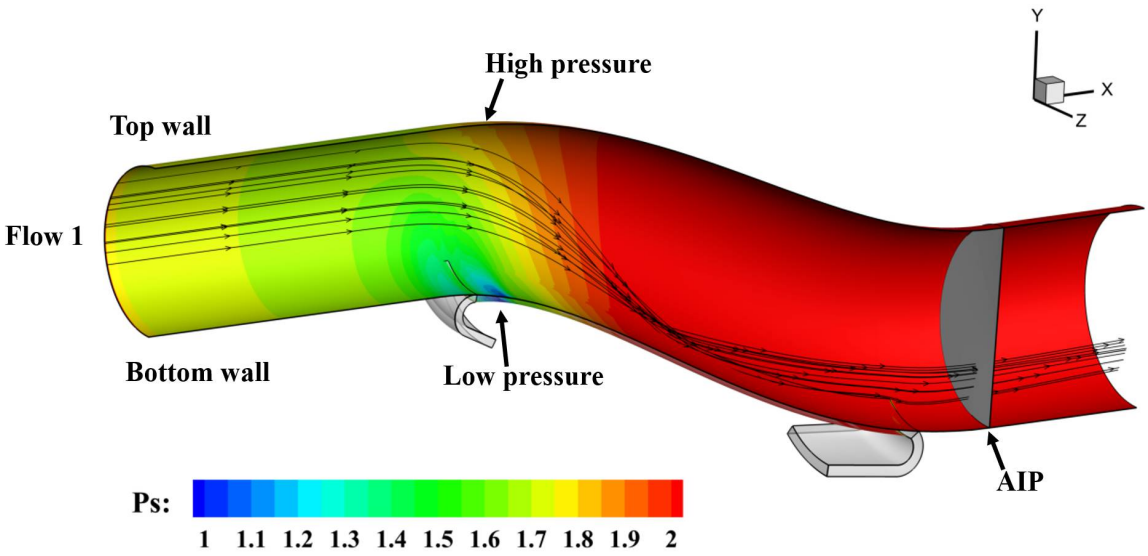

Figure 9: Wall static pressure distribution of Case 1

Fig. 10 shows the Mach number contours and streamlines of Case 3 and 4 at the symmetric plane with injection and suction β angle increased to 100° and 90° respectively. The suction location at 3.29 X/R_i (Case 4) again achieves a better performance than at 6.63 X/R_i with lower distortion and substantially reduced CFJ P_C and C_μ by 34.1% and 32.8%. Similar suction location effect is also observed in Case 1 and Case 2 with 20° smaller CFJ slot β angle. The location 3.29 X/R_i is the geometry inflection location that the slope reaches the minimum and the local diffusion reaches the maximum. Placing the suction at such location appears to be most effective to energize flow boundary layer and prevents separation onset. This is consistent with the conclusions from the other study applying the CFJ to the NASA hump and a wind turbine airfoil [31, 50]. Due to its high effectiveness, placing the suction at the inflection point also requires lower C_μ and power. Placing the suction at 6.63 X/Ri in the fully separated region is not effective because the boundary layer loss is too much. It requires very high energy cost to remove the flow separation in that case. It is more efficient to energize the boundary layer before it is "too late" when the flow is severely deteriorated. The inflection point appears to be an efficient and effective point either applying a suction of injection.

Fig. 11 shows the total pressure contours at different stream-wise cross sections. The Case 4 with the suction location at the inflection point 3.29 X/R_i effectively energizes the boundary layer and removes the flow separation. The distortion is substantially reduced as shown in Fig. 12.

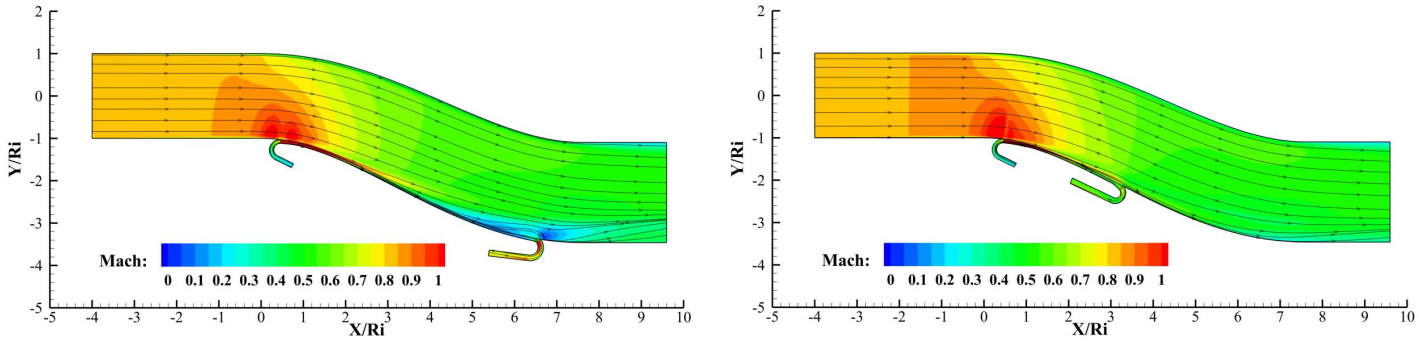

(a) Case 3, suction at 6.63 X/R_i (b) Case 4, suction at 3.29 X/R_i

Figure 10: Mach contours of the CFJ S-ducts at symmetry view, suction β=90°

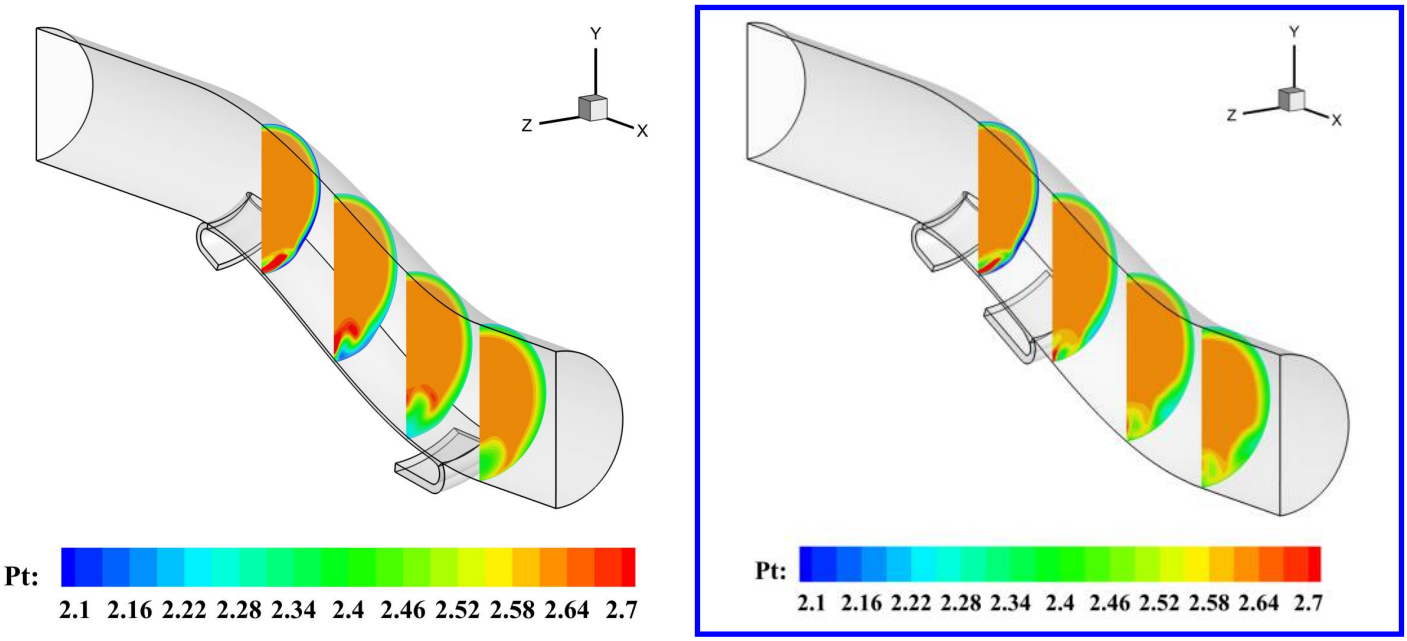

(a) Case 3, suction at 6.63 X/R_i (b) Case 4, suction at 3.29 X/R_i

Figure 11: Total pressure contours along stream-wise of CFJ S-ducts, suction β=90 °

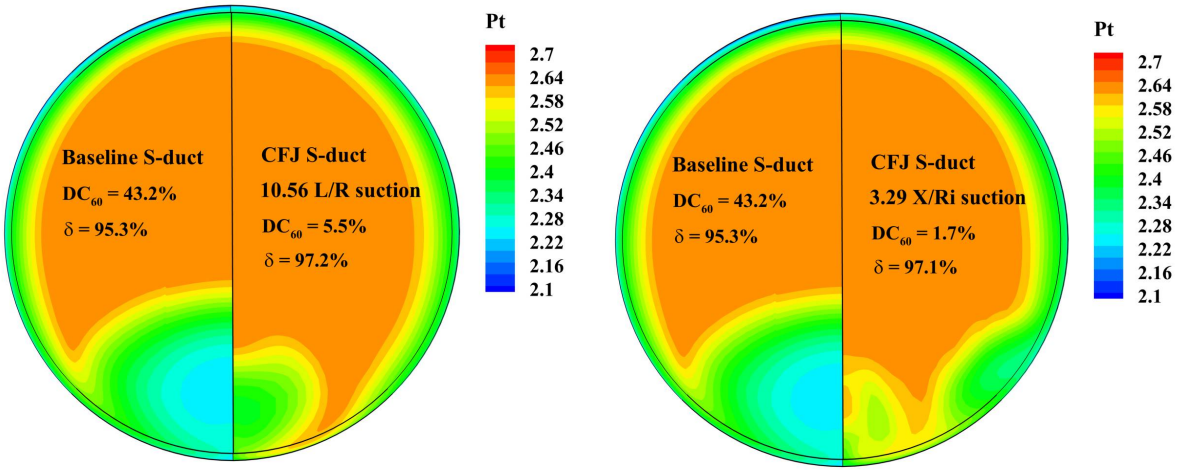

(a) Case 3, suction at 6.63 X/R_i (b) Case 4, suction at 3.29 X/R_i

Figure 12: Total pressure contours at AIP of CFJ S-ducts, suction β=90°

The performance of CFJ cases (1-4) and the baseline S-duct at AIP is presented in Table 2, where δ is the total pressure recovery and Γ is the required total pressure ratio of the CFJ micro-compressor actuator. $\Delta\delta$ is the improvement of total pressure recovery in percentage, and ΔDC_{60} measures the reduction of distortion coefficient in percentage. Table 2 indicates that all the CFJ S-ducts are very effective to reduce the flow distortion and improves the total pressure recovery. With the same C_μ, the DC_{60} of Case 2 is 56.4% lower than Case 1 due to the optimum suction location at the inflection point. The lowest DC_{60} is achieved by Case 4 with the DC_{60} reduced by about 96.1%. At the same time, the CFJ power coefficient P_C required by Case 4 is also the lowest, substantially reduced by 32.8% and 34.1% respectively compared with the Case 1, 2 and 3.

Table 2: Performance of CFJ and baseline S-ducts at AIP

Cases	C_μ	δ	$\Delta\delta$	DC_{60}	ΔDC_{60}	Γ	P_C
Baseline	-	95.3%	-	43.2%	-	-	-
CFJ-1	1.1	97.1%	1.9%	9.4%	-78.2%	1.80	0.85
CFJ-2	1.1	97.3%	2.1%	4.1%	-90.5%	1.73	0.85
CFJ-3	0.85	97.2%	2.0%	5.5%	-87.3%	1.94	0.88
CFJ-4	0.58	97.1%	1.9%	1.7%	-96.1%	1.64	0.58

7 Acknowledgment

The authors would like to acknowledge the computing resource provided by the Center for Computational Sciences at the University of Miami.

Disclosure: The University of Miami and Dr. Gecheng Zha may receive royalties for future commercialization of the intellectual property used in this study.

8 Conclusions

This paper implements Co-flow Jet (CFJ) active flow control (AFC) on the M2129 serpentine duct for mitigating flow separation with low energy consumption. Various locations and slot widths of CFJ suction duct are studied and the energy expenditure of each case is analyzed. The 3D Reynolds Averaged Navier-Stokes (RANS) equations with one-equation Spalart-Allmaras turbulence model is used. The experimental data of AGARD test case 3.1, which has throat Mach number of 0.79, is used for validation. The predicted total pressure recovery agrees very well with the experiment with the discrepancy of less than 1%. The distortion coefficient (DC_{60}) is also in an acceptable agreement with the experiment. The simulation result is further validated using the wall static pressure distribution, which also achieves a good agreement with the experiment. For the CFJ S-duct, a horn shaped slot geometry is adopted for the CFJ injection and suction slots to minimize the separation caused by CFJ sides wall. A trade study is done to investigate the circumferential width of the CFJ slots and axial position. For all the cases, the injection slot width angle is 10° more than that of the suction slot to make the two slot aligned at the same span position from the top projection view. The results show that the optimum configuration, Case 4 has the suction slot located at duct geometry inflection point with a wide suction slot width of 90°. The different CFJ configuration yields very different CFJ power consumption. Overall, the CFJ is demonstrated numerically to be very effective to mitigate the S-duct flow distortion and improve total pressure recovery. For the optimum configuration of the CFJ S-duct, a small distortion coefficient of 1.7% is achieved with the averaged total pressure recovery increased by 1.9%.

References

[1] K. A. Geiselhart, D. L. Daggett, R. Kawai, and D. Friedman, "Blended wing body systems studies: boundary layer ingestion inlets with active flow control." NASA Technical Report, NASA/CR-2003-212670, Langley Research Center; Hampton, VA, December 01, 2003.

[2] R. T. Kawai, D. M. Friedman, and L. Serrano, "Blended wing body (bwb) boundary layer ingestion (bli) inlet configuration and system studies." NASA Technical Report, NASA/CR-2006-214534, Langley Research Center; Hampton, VA, December 01, 2006.

[3] J. D. Mattingly, W. H. Heiser, and D. T. Pratt, *Aircraft engine design*. American Institute of Aeronautics and Astronautics, 2002.

[4] D. Miller and G. Addington, "Aerodynamic flowfield control technologies for highly integrated airframe propulsion flowpaths," in *2nd AIAA Flow Control Conference, AIAA 2004-2625, June 2004*.

[5] B. REICHERT and B. WENDT, "An experimental investigation of s-duct flow control using arrays oflow-profile vortex generators," in *31st Aerospace Sciences Meeting, AIAA 1993-0018, Reno,NV,11 January 1993 - 14 January*, 1993.

[6] B. H. Anderson and J. Gibb, "Study on vortex generator flow control for the management of inlet distortion," *Journal of Propulsion and Power*, vol. 9, no. 3, pp. 422–430, 1993.

[7] J. Gibb and M. Jackson, "Some preliminary results from tests using vortex generators in the circular/circular diffusing s-duct model m2129 test phase 3," *Defense research agency Rept. AP4 (92) WP15*, 1992.

[8] J. Gibb and B. Anderson, "Vortex flow control applied to aircraft intake ducts," in *Proceedings of the Royal Aeronautical Society Conf., High Lift and Separation Control, Paper*, no. 14, 1995.

[9] B. H. Anderson and J. Gibb, "Vortex-generator installation studies on steady-state and dynamic distortion," *Journal of aircraft*, vol. 35, no. 4, pp. 513–520, 1998.

[10] A. Jirasek, "Design of vortex generator flow control in inlets," *Journal of Aircraft*, vol. 43, no. 6, pp. 1886–1892, 2006.

[11] J. Yi, C. Kim, and B. J. Lee, "Adjoint-based design optimization of vortex generator in an s-shaped subsonic inlet," *AIAA journal*, vol. 50, no. 11, pp. 2492–2507, 2012.

[12] T. J. Burrows, Z. Gong, B. Vukasinovic, and A. Glezer, "Investigation of trapped vorticity concentrations effected by hybrid actuation in an offset diffuser," in *54th AIAA Aerospace Sciences Meeting, AIAA 2016-0055, San Diego, California*, 2016.

[13] T. J. Burrows, B. Vukasinovic, and A. Glezer, "Flow dynamics effected by active flow control in an offset diffuser," in *2018 Flow Control Conference, AIAA 2018-4024, June 25-29, Atlanta, Georgia*, 2018.

[14] N. A. Harrison, J. Anderson, J. L. Fleming, and W. F. Ng, "Active flow control of a boundary layer-ingesting serpentine inlet diffuser," *Journal of Aircraft*, vol. 50, no. 1, pp. 262–271, 2013.

[15] N. A. Harrison, *Active Flow Control of a Boundary Layer Ingesting Serpentine Diffuser*. Virginia Tech, 2005.

[16] I. Rudin, E. Arad, and J. Cohen, "Performance enhancement of boundary layer ingesting inlet using active flow control methods," in *2018 Applied Aerodynamics Conference,AIAA 2018-3066,Atlanta, Georgia, June 25-29*, 2018.

[17] G.-C. Zha, B. F Carroll, C. D. Paxton, C. A. Conley, and A. Wells, "High-performance airfoil using coflow jet flow control," *AIAA journal*, vol. 45, no. 8, pp. 2087–2090, 2007.

[18] A. Lefebvre, B. Dano, W. Bartow, M. Fronzo, and G. Zha, "Performance and energy expenditure of coflow jet airfoil with variation of mach number," *Journal of Aircraft*, vol. 53, no. 6, pp. 1757–1767, 2016.

[19] G. Zha, W. Gao, and C.D. Paxton, "Jet Effects on Co-Flow Jet Airfoil Performance," *AIAA Journal*, vol. 45, pp. 1222–1231, 2007.

[20] G.-C. Zha, C. Paxton, A. Conley, A. Wells, nd B. Carroll, "Effect of Injection Slot Size on High Performance Co-Flow Jet Airfoil," *AIAA Journal of Aircraft*, vol. 43, pp. 987–995, 2006.

[21] B. Wang, B. Haddoukessouni, J. Levy, and G.-C. Zha, "Numerical investigations of injection-slot-size effect on the performance of coflow jet airfoils," *Journal of Aircraft*, vol. 45, no. 6, pp. 2084–2091, 2008.

[22] B. P. E. Dano, D. Kirk, and G.-C. Zha, "Experimental Investigation of Jet Mixing Mechanism of Co- Flow Jet Airfoil." AIAA-2010-4421, 5th AIAA Flow Control Conference, Chicago, IL, 28 Jun - 1 Jul 2010.

[23] B. Dano, G. Zha, and M. Castillo, "Experimental study of co-flow jet airfoil performance enhancement using discreet jets." AIAA Paper 2011-941, 49th AIAA Aerospace Sciences Meeting including the New Horizons Forum and Aerospace Exposition, Orlando, Florida, 04 January 2011 - 07 January 2011.

[24] Lefebvre, A. and Zha, G.-C. , "Design of High Wing Loading Compact Electric Airplane Utilizing Co-Flow Jet Flow Control." AIAA Paper 2015-0772, AIAA SciTech2015: 53nd Aerospace Sciences Meeting, Kissimmee, FL, 5-9 Jan 2015.

[25] Liu, Z.-X. and Zha, G.-C., "Transonic Airfoil Performance Enhancement Using Co-Flow Jet Active Flow Control." AIAA Paper 2016-3066, AIAA Aviation, Washington, D.C., June 13-17 2016.

[26] Lefebvre, A. and Zha, G.-C., "Trade Study of 3D Co-Flow Jet Wing for Cruise Performance." AIAA Paper 2016-0570, AIAA SCITECH2016, AIAA Aerospace Science Meeting, San Diego, CA, 4-8 January 2016.

[27] G. Zha, Y. Yang, Y. Ren, and B. McBreen, "Super-lift and thrusting airfoil of coflow jet actuated by micro-compressors," in *2018 Flow Control Conference, AIAA 2018-3061, Atlanta, Georgia, June 25-29*, 2018.

[28] J. Zhang, K. Xu, Y. Yang, Y. Ren, P. Patel, and G. Zha, "Aircraft control surfaces using co-flow jet active flow control airfoil." AIAA Paper 2018-3067, 2018 Applied Aerodynamics Conference, Atlanta, Georgia, June 25-29, 2018.

[29] K. Xu and G. Zha, "High control authority 3d aircraft control surfaces using co-flow jet," in *AIAA Aviation 2019 Forum, Dallas, AIAA 2019-3168, Texas, 17-21 June*, 2019.

[30] K. Xu, J. Zhang, and G. Zha, "Drag minimization of co-flow jet control surfaces at cruise conditions." AIAA 2019-1848, AIAA Scitech 2019 Forum, San Diego, California, 7-11 January 2019.

[31] K. Xu, Y. Ren, and G. Zha, "Numerical investigation of nasa hump using co-flow jet for separation control." AIAA Paper will be presented in 2020 AIAA SciTech Forum, Orlando, Florida, 6C10 January, 2020.

[32] Lefebvre, A. and Dano, B. and Bartow, W. and Di Franzo, M. and Zha, G.-C., "Performance Enhancement and Energy Expenditure of Co-Flow Jet Airfoil with Variation of Mach Number." AIAA Paper 2013-0490, AIAA Journal of Aircraft, DOI: 10.2514/1.C033113, 2016.

[33] Y. Wang and G.-C. Zha, "Study of 3D Co-flow Jet Wing Induced Drag and Power Consumption at Cruise Conditions." AIAA Paper 2019-0034, AIAA SciTech 2019, San Diego, CA, January 7-11, 2019.

[34] Y. Wang and G.-C. Zha, "Study of Super-Lift Coefficient of Co-Flow Jet Airfoil and Its Power Consumption." Submitted to AIAA Aviation 2019, AIAA Applied Aerodynamics Conference, Dallas, Texas, 17-21 June 2019.

[35] P. Spalart and S. Allmaras, "A One-equation Turbulence Model for Aerodynamic Flows." AIAA-92-0439, 30th Aerospace Sciences Meeting and Exhibit, Reno,NV,U.S.A., 06 January 1992 - 09 January 1992.

[36] Y.-Q. Shen, G.-C. Zha, and B.-Y. Wang, "Improvement of Stability and Accuracy of Implicit WENO Scheme ," *AIAA Journal*, vol. 47, pp. 331–344, 2009.

[37] Shen, Y.-Q. and Zha, G.-C. and Chen, X.-Y., " High Order Conservative Differencing for Viscous Terms and the Application to Vortex-Induced Vibration Flows," *Journal of Computational Physics*, vol. 228(2), pp. 8283–8300, 2009.

[38] Shen, Y.-Q. and Zha, G.-C. , " Improvement of the WENO Scheme Smoothness Estimator," *International Journal for Numerical Methods in Fluids*, vol. DOI:10.1002/fld.2186, 2009.

[39] G.-C. Zha, Y. Shen, and B. Wang, "An improved low diffusion E-CUSP upwind scheme ," *Journal of Computer & Fluids*, vol. 48, pp. 214–220, 2011.

[40] G.-C. Zha and E. Bilgen, "Numerical study of three-dimensional flows using unfactored upwind-relaxation sweeping algorithm," *Journal of Computational Physics*, vol. 125, no. 2, pp. 425–433, 1996.

[41] B. Wang, Z. Hu, and G.-C. Zha, "General subdomain boundary mapping procedure for structured grid implicit cfd parallel computation," *Journal of Aerospace Computing, Information, and Communication*, vol. 5, no. 11, pp. 425–447, 2008.

[42] B. Wang and G.-C. Zha, "Detached-eddy simulation of a coflow jet airfoil at high angle of attack," *Journal of aircraft*, vol. 48, no. 5, pp. 1495–1502, 2011.

[43] Y. Yang and G. Zha, "Super-lift coefficient of active flow control airfoil: What is the limit?." AIAA Paper 2017-1693, AIAA SCITECH2017, 55th AIAA Aerospace Science Meeting, Grapevine, January 9-13 2017.

[44] Im, H.-S. and Zha, G.-C. and Dano, B. P. E., "Large Eddy Simulation of Coflow Jet Airfoil at High Angle of Attack," *Journal of Fluid Engineering, vol. 136(2), p. 021101*, 2014.

[45] J. Dudek, "S-duct inlet with and without vortex generator validation cases." NPARC Alliance Verification and Validation Archive, https://www.grc.nasa.gov/WWW/wind/valid/sduct/sduct.html, 02 Mar 2009.

[46] A. G. F. A. RESEARCH and DEVELOPMENT, "Air intakes for high speed vehicles." Fluid Dynamics Panel Working Group 13, AR-270, Fort Worth, TX,, Sep 1991.

[47] J. C. Dudek, "Empirical model for vane-type vortex generators in a navier-stokes code," *AIAA journal*, vol. 44, no. 8, pp. 1779–1789, 2006.

[48] J. C. Dudek, "Modeling vortex generators in a navier-stokes code," *AIAA journal*, vol. 49, no. 4, pp. 748–759, 2011.

[49] J. Seddon and E. Goldsmith, *Intake Aerodynamics*. AIAA Inc., New York, 1985.

[50] K. Xu and G. Zha, "Investigation of coflow jet active flow control for wind turbine airfoil." AIAA Paper will be virtually presented in 2020 AIAA AVIATION Forum and Exposition, 15C19 June, 2020.